

# Available online at www.sciencedirect.com The state of t

journal homepage: www.elsevier.com/locate/jmrt



# **Original Article**

# Feasibility of multilayer solid-state deposition via lateral friction surfacing for metal additive manufacturing



Ebrahim Seidi\*, Scott F. Miller

Department of Mechanical Engineering, University of Hawaii at Manoa, Honolulu, HI, USA

#### ARTICLE INFO

Article history:
Received 7 March 2022
Accepted 27 July 2022
Available online 4 August 2022

Keywords:
Additive manufacturing
Solid-state deposition
Material characterization
Thin coating
Infrared thermography

Multilayer deposition

#### ABSTRACT

Lateral friction surfacing is a novel solid-state deposition process in which the radial surface of the rotating consumable tool is forced into the substrate surface, facilitating material transfer. This technique is an excellent alternative to create thin and ultrasmooth metallic deposit layers for repairing damaged surfaces or improving corrosion and wear resistance. The lateral friction surfacing approach results in a deposition process with lower generated process temperatures than conventional friction surfacing, which leads to reducing thermal effects on the microstructures and mechanical properties of the deposits. In this study, the extent of material transfer to the substrate was explored via multiple passes of the tool in an effort to create multiple layers of deposited material. Two types of substrate plates with different surface roughness as well as two different strategies for employing the consumable tools were experimented. A comprehensive assessment through conducting real-time force measurement, surface roughness measurement, hardness testing, optical microscopy, infrared thermography, scanning electron microscopy, and EDS analysis was performed to characterize the process and the fabricated deposits. The thickness of the coating was found to vary through work material transfer to the substrate and reverse material transfer from the coating to the radial surface of the rod, resulting in an approximately steady-state deposit thickness. The reverse material transferring process from the coating to the radial surface of the rod through rubbing off the previously fabricated coatings limits plasticizing more consumable material and built-up

© 2022 The Author(s). Published by Elsevier B.V. This is an open access article under the CC BY license (http://creativecommons.org/licenses/by/4.0/).

## 1. Introduction

The friction surfacing (FS) technique is a thermomechanical friction-based additive manufacturing approach that can be utilized for solid-state metal deposition from a consumable tool onto a metallic substrate surface [1]. In this approach, a rotating consumable tool is forged against the substrate surface, resulting in frictional heat generation at the tool/

E-mail address: seidi@hawaii.edu (E. Seidi).

<sup>\*</sup> Corresponding author.

substrate interface. During the dwell time, the frictional heat provides enough energy to plasticize the consumable material before the deposition process begins. Then, the consumable rod traverses along the surface of the substrate to fabricate the first layer of the coating [2]. Since the frictional force and heat generated at the interface of the tool and substrate tends to zero as the material reaches the temperatures near the melting point, the maximum process temperature achieved is restricted by the melting point temperature, resulting in a solid-state deformation condition [3].

With this approach, fabricating high-quality coatings are possible for a wide range of combination materials for tool/ substrate; however, aluminum and steel alloys have been studied much more frequently and thoroughly than any other material [4]. There are investigations in which the same alloy has been employed as both tool and substrate materials, including alloys of aluminum [5-7], steel [8], and titanium [9,10]; however, the majority of the published studies are mostly focused on different combinations of aluminum and steel alloys as tool/substrate materials [4]. Various process parameters such as tool rotational speed, axial force, and traverse speed are controlling variables and significantly affect the result. The effects of process factors on the process temperature [11,12], surface roughness [13], surface hardness [14,15], wear resistance performance [8,16], corrosion performance [17,18], residual stress [10,19], grain boundaries and microstructures [20,21], and the coating geometry [22-24] have been studied.

A fine-grained, thick layer can be deposited on a substrate in FS, which has potential for multilayer deposition and additive manufacturing of metal-matrix composites. For this purpose, the first deposited layer undergoes a machining process to provide a flat surface for the second layer of coating to be deposited. This procedure should be repeated to build up a three-dimensional metallic sample with the desired height [1,25]. In cases, where a specimen with a width larger than tool diameter is required, multiple adjacent coating tracks should be deposited to create each layer of the coating. This approach has been successfully employed by Dilip et al. as an additive manufacturing technique to create a 3D part [26]. In order to develop a 3D part, they fabricated five, four, and three adjacent tracks in the first, second, and third deposited layers, respectively. In another investigation, the multi-layer FS deposition process was performed for additive manufacturing of a 3D composite part made of aluminum reinforced by titanium particles [27]. Five holes were made in the AA5083-H112 consumable tool and filled with titanium powder. The results of the study exhibited strong bonds between deposited layers, and uniform distribution of titanium particles in the developed part.

Tokisue et al. investigated the monolayer and double layer friction surfaced AA2017 coatings onto AA5052 substrate to evaluate the influences of process factors on the mechanical and microstructural properties [28]. The efficiency of the double-pass deposition was higher than the single-pass deposition. Furthermore, the hardness of deposited coatings in the monolayer and double layer deposition was the same as

as-received material, while the strength of the double layer was higher than the monolayer deposit. In another study by Pereira et al. [8], multi-layer adjacent coatings of AISI H13, AISI 1024, and AISI 1045 were deposited onto a mild steel substrate. The aim of this process was to provide an adequate deposited area for the pin-on-disc wear testing, and AISI 1024 deposit had a better wear resistance due to its lower wear friction coefficient.

FS has been employed in the additive friction stir deposition technique [29]. In this technique, the solid consumable rod or powder feed material is delivered to the processing zone through a non-consumable rotating hollow metallic shoulder under pressing load. The frictional heat developed at the interfaces between material and shoulder results in softening and plasticizing of the feeding material and deposition of the coating [30,31]. During the deposition process, the majority of the plastic work is turned to heat energy, further developing of heat energy generation mechanism [32]. Without melting or rapid solidification during the process, this solid-state deposition technique enables fabricating metallic materials with minimal hot cracking, porosity, residual stresses, and distortion [33]. The additive friction stir deposition approach has been employed for fabricating different metallic materials such as aluminum [34-37], copper [36,38], Inconel [39,40], titanium [41], magnesium [42]. The hollow tool shoulders made of tool steel can be utilized to deposit low strength materials; however, tungsten carbide or polycrystalline cubic boron nitride are required for deposition of high strength materials [43].

Lateral friction surfacing (LFS) is a new approach in FS, in which the side of the consumable rod is forged against the substrate surface instead of the end of the tool. Due to the frictional heat generated at the interface, the material softening starts, and material transferring process happens from the side of the consumable tool onto the substrate surface [44]. The influence of process parameters of LFS on the resulting coating properties was investigated in [44,45]. The influence of crucial process parameters such as normal force and tool rotational speed on the deposition of single-layer coating of different aluminum alloys was investigated in [46]. More investigations on characterization [47] and corrosion performance [48] of the deposited materials through this technique have been conducted.

Based on previous studies, it has been observed that multiple passes are beneficial for complete coverage of deposition and further addition of material onto the substrate. Therefore, the goal of this study is to characterize the feasibility of multiple layers of material through LFS. The hypothesis is that multilayer deposition will result in increased coating thickness. Therefore, multilayer deposition of the LFS technique was assessed for additive manufacturing purposes. In this approach, multiple thin coating layers can be fabricated on previously deposited layers. The results of multiple tool passes were completely characterized and presented in this paper. Several analyses such as real-time force measurement, coating surface roughness measurement, infrared thermography, optical microscopy, scanning electron microscopy

(SEM), and EDS were conducted to characterize the process and the deposited coatings.

#### 2. Materials and methods

## 2.1. Materials, equipment, and setup

Multilayer deposition of AA6061 onto AISI 1018 and AISI 4140 was performed by LFS, which may be ultimately utilized for additive manufacturing purposes. The physical properties and chemical composition of the consumable and substrate materials are presented in Table 1. There are no retreating and advancing sides in the LFS, and all points on the lateral surface of the consumable rod undergo a constant rotational speed when the tool comes to contact with the substrate, as shown in Fig. 1. Therefore, more consistent deposits can be made with LFS versus conventional FS.

Multilayer deposition of AA6061 consumable rod was conducted using two different strategies. In the first strategy, a single tool has been employed to fabricate each multilayer sample deposit regardless of the number of its passes. In the multi-tool strategy, a new rod has been utilized to fabricate each pass in each multilayer deposit. No critical difference in the deposition results was observed due to changing the substrate material in the single-tool strategy, showing that the influence of substrate material and surface roughness were not noteworthy. Therefore, only one material was employed as the substrate material in the multi-tool strategy.

# 2.2. Deposition process, parameters, and temperature measurement

The LFS technique involves complex material transferring and deformation; therefore, there is a need to precisely control the process parameters. A customized JET JMD-18 Mill/Drill machine with a servo power feed was the platform for the experiments. A uniform and precise longitudinal table movement during the process was guaranteed by equipping the machine's table with the servo power feed. The tool was forced into the substrate for a dwell period of 20 s to achieve appropriate process temperature before lateral feed. After the dwell phase, the tool moved at a constant horizontal feeding rate of 44 mm/min. The normal force was manually controlled during the deposition process. Normal and tangential forces were measured and recorded with a Kistler 9272 drilling dynamometer attached to the clamping vise on the table, data acquisition system, and LabVIEW. The process parameters of the experiment are summarized in Table 2.

Temperature was measured with an IR FLIR SC655 camera capable of measuring temperatures in the range from -20 to 650 °C. This measuring technique provides a convenient and non-contact procedure to record the temperature based on the radiance from the tool/substrate interface. Since FS is a solid-state process, deposition happens at a temperature less than the melting point temperature of the consumable material. In this study, the measuring range of the IR camera perfectly covers the maximum process temperature for

AA6061-T6         Physical Property:         UTS         Melting Point         Thermal Conductivity           Values:         310 MPa         588 °C         167 W/m.K           Elements:         6 C         Cr         Mn         An           AISI 1018         % of composition:         0.7         0.4-0.8         0.15-0.4         0.15         0.25           AISI 1018         Physical Property:         UTS         Melting Point         Thermal Conductivity           AISI 1018         Physical Property:         Po.040         0.60-0.90         0.14-0.20           AISI 4140         Physical Property:         UTS         Melting Point         Thermal Conductivity           AISI 4140         Physical Property:         UTS         Melting Point         42.6 W/mK           AISI 4140         C         Physical Property:         C         A2.6 W/mK           AISI 41	Table 1 – Phys	Table 1 $-$ Physical properties and chemical composition of	mical composi		AA6061-T6 [46], AISI 1018 [46], and AISI 4140 [49].	18 [46], and AIS	1 4140 [49].				
Values:         310 MPa         Si8 °C           Elements:         Fe         Si         Cr         Cu           % of composition:         0.7         0.4-0.8         0.04-0.35         0.15-0.4           Physical Property:         UTS         Melting Point         Additional         Mn           Values:         P         Mn         Additional         Mn           % of composition:         \$         \$         0.60-0.90         Melting Point           Values:         655 MPa         1416 °C         P           Values:         Gr         Si         C           Elements:         Cr         Si         C           % of composition:         0.8-1.1         0.15-0.3         0.38-0.43         0.035	AA6061-T6	Physical Property:	UTS		Melting Point		Thermal Co	nductivity		Elongation at Break	: Break
Elements:         Fe         Si         Cu           % of composition:         0.7         0.4-0.8         0.04-0.35         0.15-0.4           Physical Property:         UTS         Melting Point         1480 °C         0.15-0.4           Values:         P         Mn         1480 °C         0.00-0.90           % of composition:         \$         \$         0.60-0.90         Melting Point           Values:         655 MPa         1416 °C         Melting Point           Values:         655 MPa         1416 °C         P           Elements:         Cr         Si         C           % of composition:         0.8-1.1         0.15-0.3         0.38-0.43         0.035		Values:	310 MPa		288 °C		167 W/m.K			17%	
% of composition:         0.7         0.4—0.8         0.04—0.35         0.15—0.4           Physical Property:         UTS         Melting Point         Action           Values:         440 MPa         1480 °C         Action           % of composition:         50.040         0.60—0.90         Action           Physical Property:         UTS         Melting Point         Action           Values:         655 MPa         1416 °C         P           Elements:         Cr         Si         C           % of composition:         0.8—1.1         0.15—0.3         0.38—0.43         0.035		Elements:	Fe	Si	Cr	Cu	Mn	Zn	Ti	Mg	Al
Physical Property:         UTS         Melting Point           Values:         440 MPa         1480 °C           Elements:         P         Mn           % of composition:         ≤0.040         0.60-0.90           Physical Property:         UTS         Melting Point           Values:         655 MPa         1416 °C           Elements:         Cr         Si           % of composition:         0.8-1.1         0.15-0.3         0.38-0.43         0.035		% of composition:	0.7	0.4-0.8	0.04-0.35	0.15-0.4	0.15	0.25	0.15	0.8-1.2	Balance
Values:         440 MPa         1480 °C           Elements:         P         Mn           % of composition:         ≤0.040         0.60-0.90           Physical Property:         UTS         Melting Point           Values:         655 MPa         1416 °C           Elements:         Cr         Si         P           % of composition:         0.8-1.1         0.15-0.3         0.38-0.43         0.035	AISI 1018	Physical Property:	UTS		Melting Point		Thermal Co	nductivity		Elongation at Break	: Break
Elements:         P         Mn           % of composition:         <0.040         0.60-0.90           Physical Property:         UTS         Melting Point           Values:         655 MPa         1416 °C           Elements:         Cr         Si         C           % of composition:         0.8-1.1         0.15-0.3         0.38-0.43         0.035		Values:	440 MPa		1480 °C		51.9 W/mK			15%	
% of composition:         ≤0.040         0.60-0.90           Physical Property:         UTS         Melting Point           Values:         655 MPa         1416 °C           Elements:         Cr         Si         C           % of composition:         0.8-1.1         0.15-0.3         0.38-0.43         0.035		Elements:	Ъ		Mn		C		S	Fe	
Physical Property:         UTS         Melting Point           Values:         655 MPa         1416 °C           Elements:         Cr         Si         P           % of composition:         0.8-1.1         0.15-0.3         0.38-0.43         0.035		% of composition:	≤0.040		0.60-090		0.14-0.20		<0.050	Balance	
655 MPa 1416 °C P P C C P P P P C P P P P P P P P P	AISI 4140	Physical Property:	UTS		Melting Point		Thermal Co	nductivity		Elongation at Break	: Break
Cr         Si         C         P           0.8-1.1         0.15-0.3         0.38-0.43         0.035		Values:	655 MPa		1416 °C		42.6 W/mK			25.70%	
0.8-1.1 0.15-0.3 0.38-0.43 0.035		Elements:	Cr	Si	C	Ъ	Mo		S	Mn	Fe
		% of composition:	0.8-1.1	0.15-0.3	0.38-0.43	0.035	0.15-0.25		0.04	0.75-1	Balance

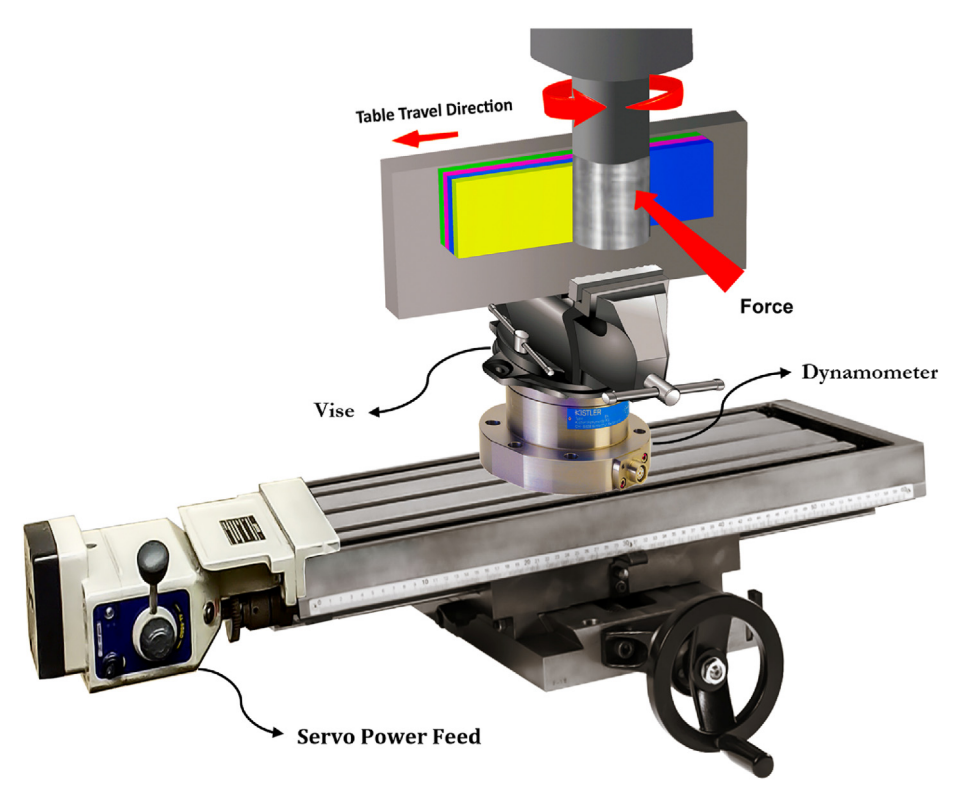


Fig. 1 – Multi-pass deposition through LFS.

fabricating AA6061 tools, which is lower than the consumable material's melting point (588 °C). For infrared thermography, the IR camera was placed at a proper distance of 50 cm from the processing zone in a way that makes an angle of 10 with the substrate while focused on the tool/substrate interface, as shown in Fig. 2. The steel substrates and consumable rods were cleaned with ethanol before the surfacing process. Afterward, the surface of the substrates was covered by a thin layer of graphite to improve the emissivity of steel substrate up to 0.80 [50].

#### 2.3. Surface characterization

After depositing the metallic layers, a Landtek SRT6200S surface roughness tester was employed to evaluate the surface roughness of the fabricated layers. The surface roughness of the substrates without coating was also measured to provide a better comparison between the roughness of deposits and asreceived substrates. Moreover, the hardness testing was performed using a Wilson Instrument hardness tester to evaluate the surface hardness of the used and as-received rods.

# 2.4. Microscopy

Further assessments of the deposited layers were performed by conducting cross-sectional optical microscopy, SEM, and EDS analyses. The cross-sectional view of the specimens comprised of the deposited multilayer coating, substrate, and the coating/substrate interface. As for sample preparation, a small piece of the deposited coatings with a length of 1 cm was cut from the middle of coatings and mounted in epoxy, as demonstrated in Fig. 3. The mounted specimens were subjected to a two-step polishing process using a cloth polishing wheel and polycrystalline diamond suspension with three different particle mean sizes of 3  $\mu$ m, 1  $\mu$ m, and 0.25  $\mu$ m.

The deposited coatings were subjected to optical microscopy and scanning electron microscopy. In order to examine the thickness of deposited coatings, samples were evaluated by utilizing a Leica DM2700 M optical microscope, which was equipped with N PLAN achromatic objective series with different magnification in the range of  $5\times$  to  $100\times$ . For an accurate observation and thickness measurement, the  $20\times$  plan achromatic objective was employed. In order to investigate the characteristics of the deposits, a scanning electron microscope type FEI Helios NanoLab 660 Dual-Beam equipped with an Oxford Instruments X-Max EDS was utilized. The SEM examination provided more information regarding the influence of multilayer deposition on the microstructures, bonding, and surface topography of the coating, while the EDS analysis yields coating composition and elemental distribution within the deposit. The SEM cross-sectional view revealed any gaps or cracks at the coating/substrate interface or between the deposited layers that significantly reduce the bonding strength and coating quality.

# 3. Results and discussion

Figures 4(a-d) and 4(e-h) present the multilayer deposits fabricated onto AISI 1018 and AISI 4140 substrate, respectively. Some uncovered regions can be seen in the figures, especially in the single and double pass deposition layer. Significantly

Table 2 — Materials, <sub>I</sub>	process parameters, and scena	arios employed in the	e experiments.		
Number of Passes	Strategies	Materials	Tool Rotational Speed	Traverse Speed	Normal Force
1, 2, 3, 4, and 10	1st—single-tool: using a single rod for depositing all layers of a sample. 2nd—multi-tool: using a new rod for depositing each layer.	Tool: AA6061 Substrate: AISI 1018 & AISI 4140	2300 rpm	44 mm/min	150 N

improved coating coverage and consistency was observed in the sample that was surfaced with 4 passes on both substrate materials.

# 3.1. Force analysis

A manually controlled normal force of 150 N was adopted to fabricate all samples during the multilayer deposition of AA6061. The measured tangential and normal forces during the dwell period of 20 s at the beginning of the first layer deposition, followed by a constant horizontal feeding rate of 44 mm/min, is shown in Fig. 5. The result revealed a higher tangential force for AISI4140 than AISI1018 substrate, which makes sense due to the higher surface roughness. The tangential forces were lower than the normal force during the deposition of the first layer; however, they increased to the same values as the normal force or even higher after a few passes, thought to be caused by increased friction from the aluminum tool interacting with the deposited aluminum.

A real-time ratio of the tangential force  $(F_t)$  and the normal force  $(F_n)$  for each pass was calculated, as presented in Fig. 6. The force ratio increased with the number of passes for both substrate materials. Higher force ratio indicates a higher friction coefficient between the rod and substrate resulting from higher generated process temperature at the interface due to further deposition passes. Typically, coefficient of friction decreases as material approaches the melting temperature and softens. In this study, it is thought that at low process temperatures, a thin layer of material is plasticized through high shearing stress. This thin layer of plasticized material is compressed between the tool and substrate and has higher contact area with the substrate surface, thereby increasing adhesive bonding and coefficient of friction. The tangential force increases until it converges to normal force

during deposition of the fourth layer. In most of the passes, the force ratio increases at the beginning of each pass and then reaches a steady state with small fluctuations.

# 3.2. Process temperature

Process temperature is a critical factor determining the quality of the deposited coatings [12]. In this investigation, a detailed thermography analysis was performed to assess the influence of multi-pass deposition on the process temperature. The process temperature at the tool/substrate interface for different number of passes was recorded, and the temperature profiles correlated to both substrate materials are

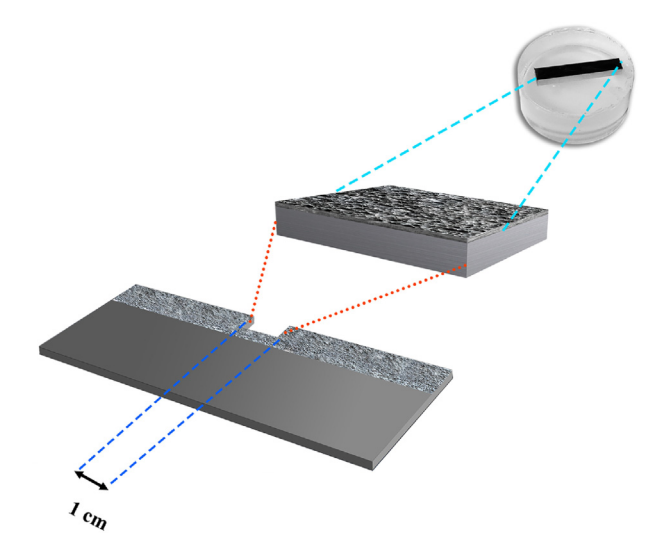


Fig. 3 - Cross section viewing of fabricated samples.

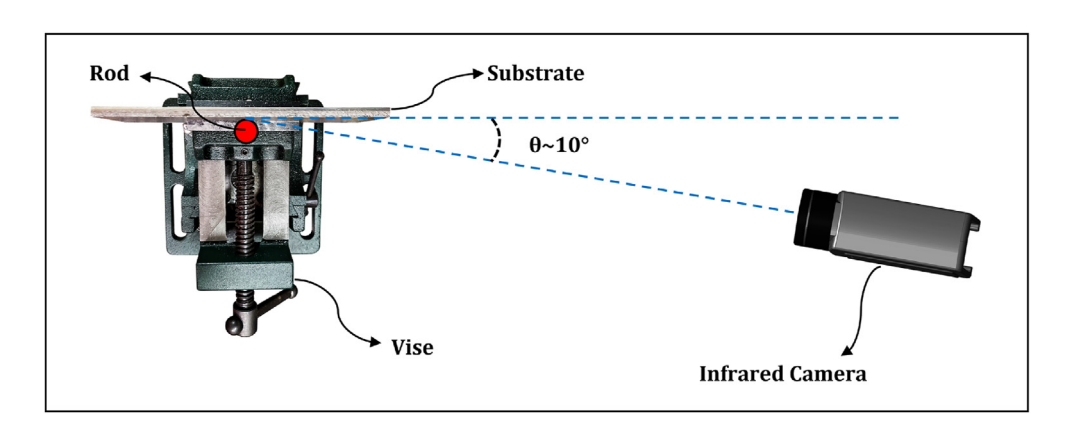


Fig. 2 – Schematic demonstration of IR thermography configuration used in the experiment.

presented in Fig. 7. An increase in the number of passes, while keeping all other process factors constant, led to higher maximum process temperatures in each deposition pass. As shown in Fig. 7., the temperature at the tool/substrate interface dropped rapidly at the completion of every pass, which exhibited a high heat dissipation rate due to the high thermal conductivity of the aluminum tool and steel substrates. However, increasing the number of passes led to more heat accumulation in the tool and substrate, which resulted in higher maximum process temperature in the next deposition pass.

The maximum process temperatures during deposition of the first coating layer onto AISI 1018 and AISI 4140 were 167.5 and 177.5 °C, respectively. This difference is mainly due to the higher surface roughness of the AISI 4140 substrate. The difference between maximum process temperatures of deposition onto these dissimilar substrates increased as the number of passes increased, as presented in Fig. 8. The maximum process temperatures of deposition onto AISI 4140 substrate were 10, 20, 56, and 60 °C higher than that in deposition onto AISI 1018 substrate during 1st, 2nd, 3rd, and 4th pass, respectively.

The maximum process temperature trends from the first to the 10th pass were very different for the two strategies. As presented in Fig. 8, the maximum process temperature decreases at some point during the single-tool strategy;

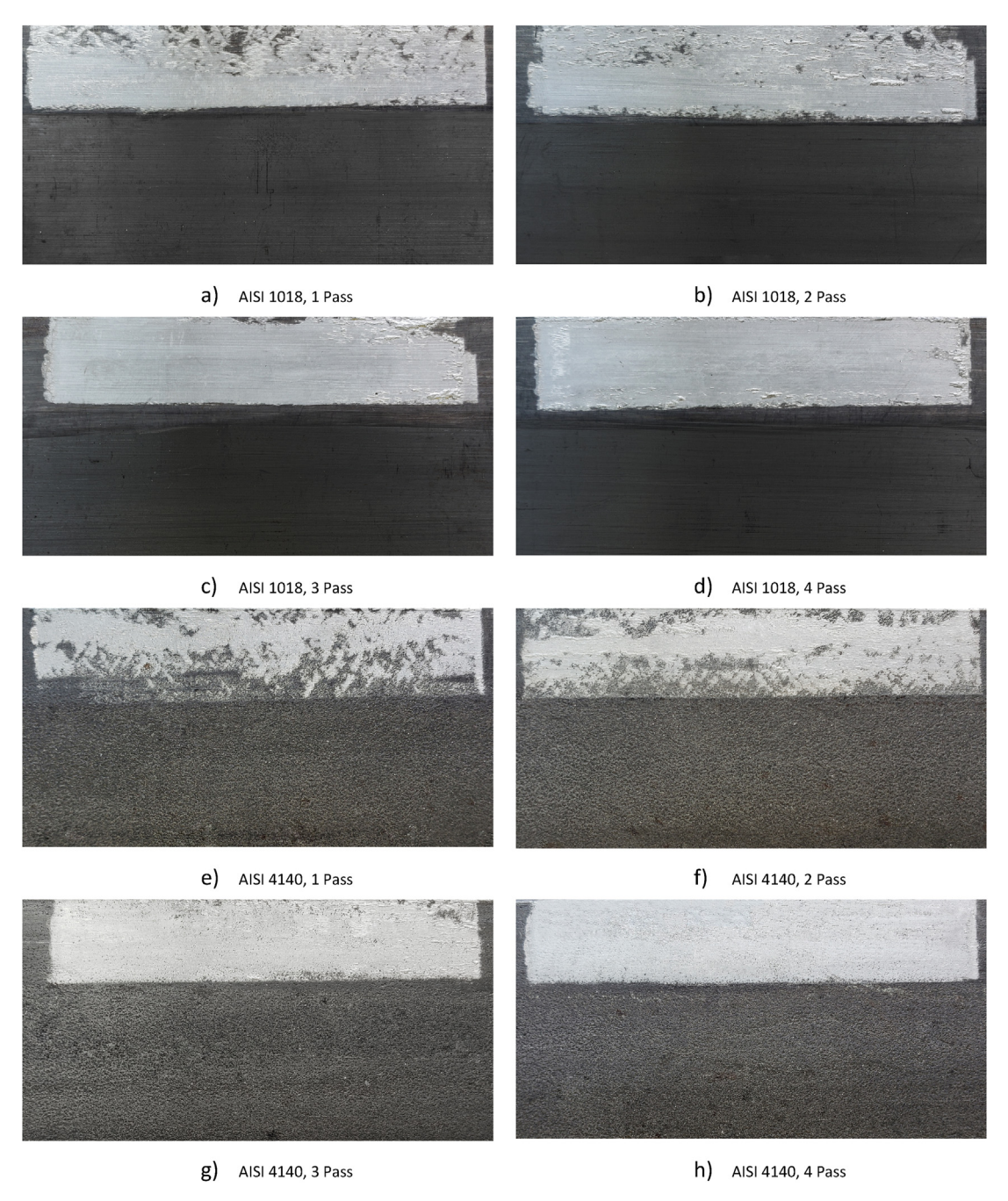


Fig. 4 - Monolayer and multilayer deposits fabricated by LFS.

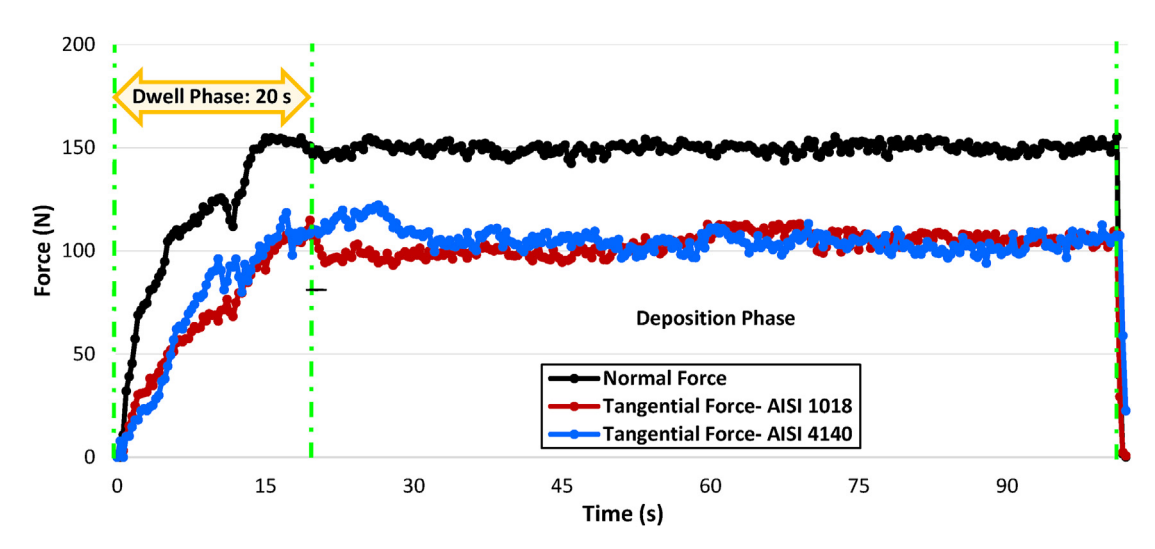


Fig. 5 - Normal and tangential forces during the deposition of first layer onto AISI 1018 and AISI 4140.

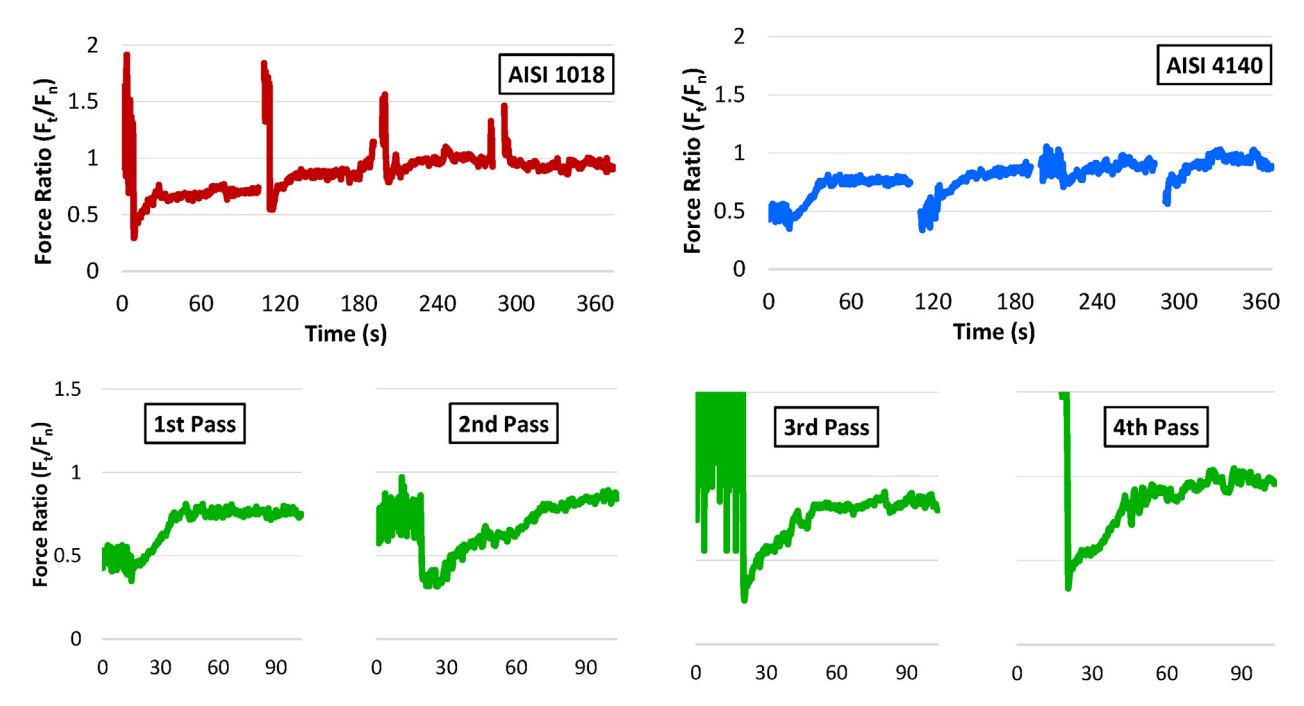
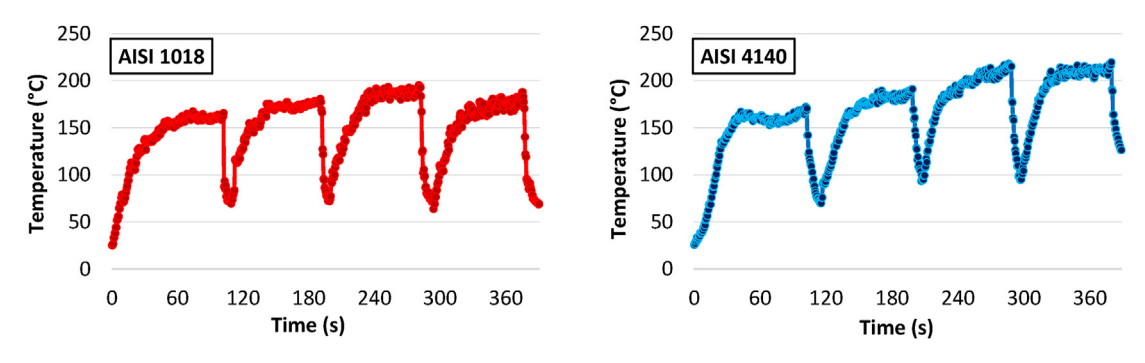


Fig. 6 - Force ratio during LFS deposition using (top) single-tool strategy, and (bottom) multi-tool strategy.



 $Fig.\ 7-Process\ temperature\ during\ LFS\ deposition\ of\ coatings\ with\ different\ number\ of\ passes.$ 

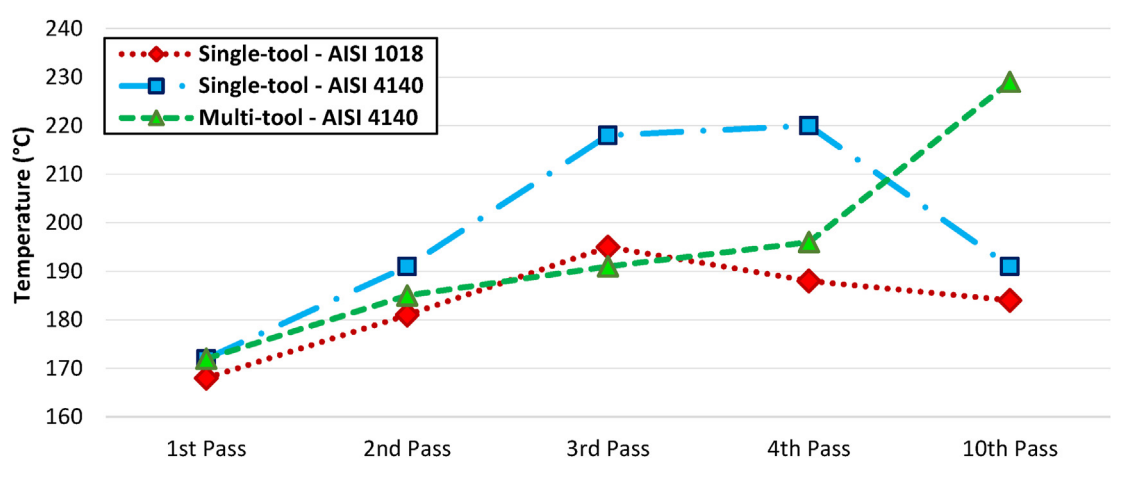


Fig. 8 - Maximum process temperature in each pass.

however, it continuously increases in the multi-tool strategy. This can be explained according to wear and material plasticization at the interface. During the deposition through the single-tool strategy, only one rod was employed in the multipass deposition process. The consumable material at the tool/ substrate interface reached higher temperatures and plasticized creating the coating. As the thin layer on the radial surface of the rod became plasticized, the coating transferred back to the radial surface of the rod, which prevented heating and deposition of more consumable material. As shown in Fig. 9, the reverse material transferring process formed a softer layer on the radial surface of the rod using the previously deposited material, which caused cracks and pores. The results of hardness testing confirm lower surface hardness values for the used rod compared to the as-received rod, as shown in Fig. 9. The plasticized material transferred back and forth between rod and substrate frequently, preventing direct contact between the hard surface beneath the plasticized

layer and the substrate surface. As a result, reduced heat generation and decreasing process temperature due to lower wear and friction between the rod and substrate were observed. The error bars in Fig. 9 show the standard deviation, derived from hardness testing results of five different random points on the radial surface of the rods. The larger error bars obtained in the 10-pass deposition process show the inconsistent surface hardness values for the used tools, which is due to the material transferred back from the coating to some areas on the surface of the tools.

On the other hand, in the multi-tool strategy, a new rod with a fresh and harder lateral surface was used for fabricating each pass. As the new rotating rod contacted the thin layer of coating, it removed the deposit and directly contacted the substrate surface, resulting in higher friction, wear, and more heat generation. The accumulation of heat in the substrate increased the substrate temperature, thus facilitating a higher process temperature in the following passes. The heat

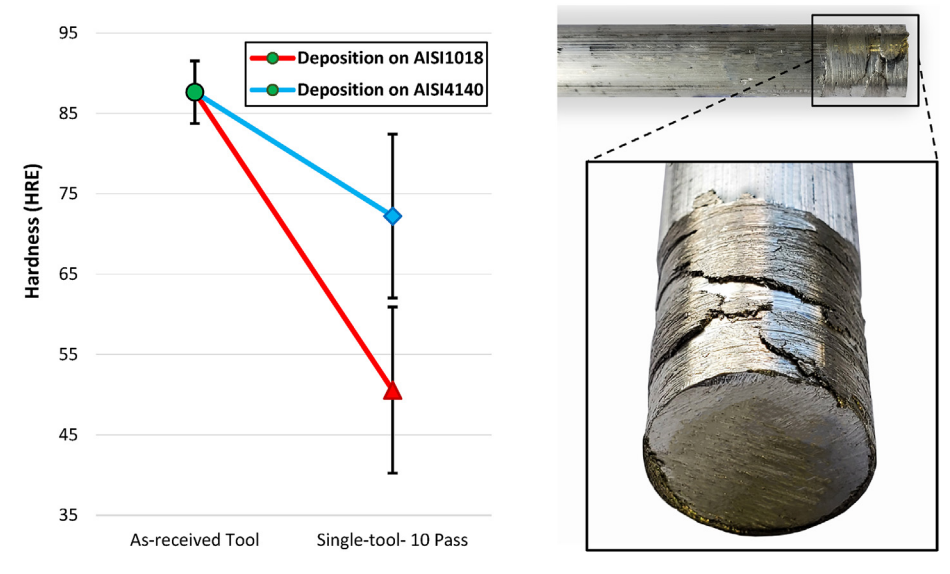


Fig. 9 - Rod after the reverse material transfer process and evolution of lateral surface hardness of the rods.

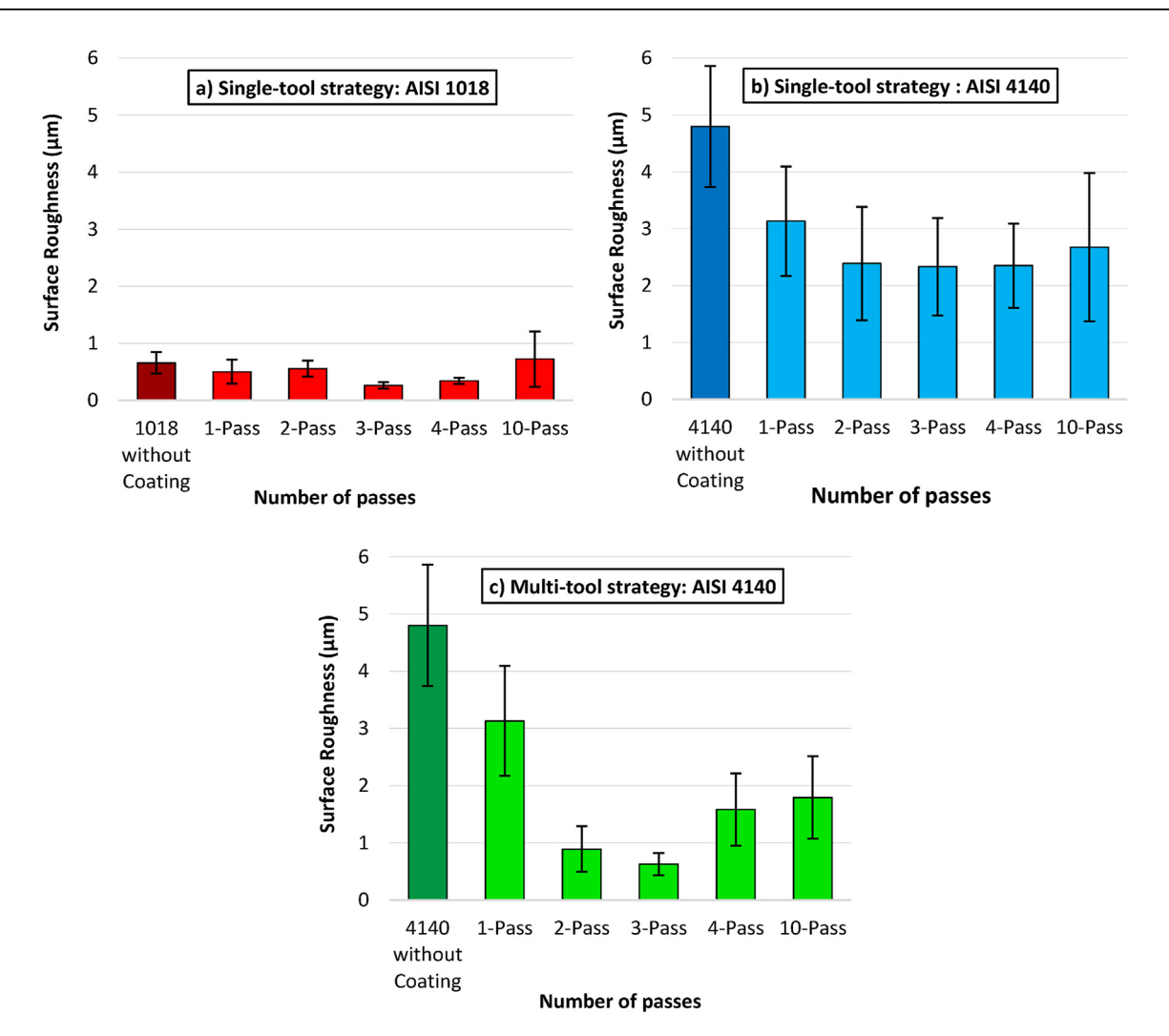


Fig. 10 - Surface roughness of coatings different number of passes provided by LFS.

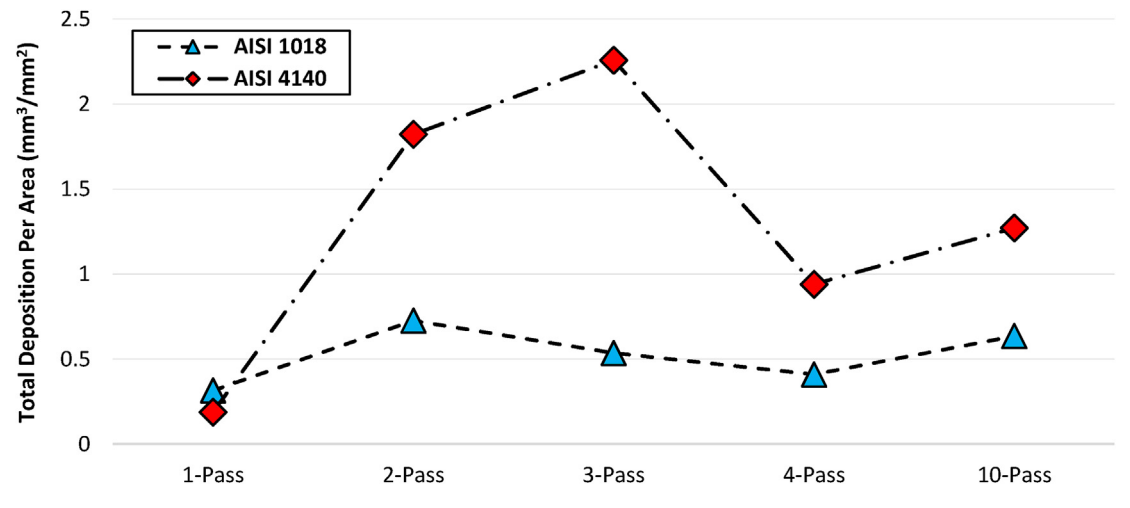


Fig.~11-Total~material~deposition~per~area~from~the~beginning~of~the~process~up~to~fabricating~of~each~pass.

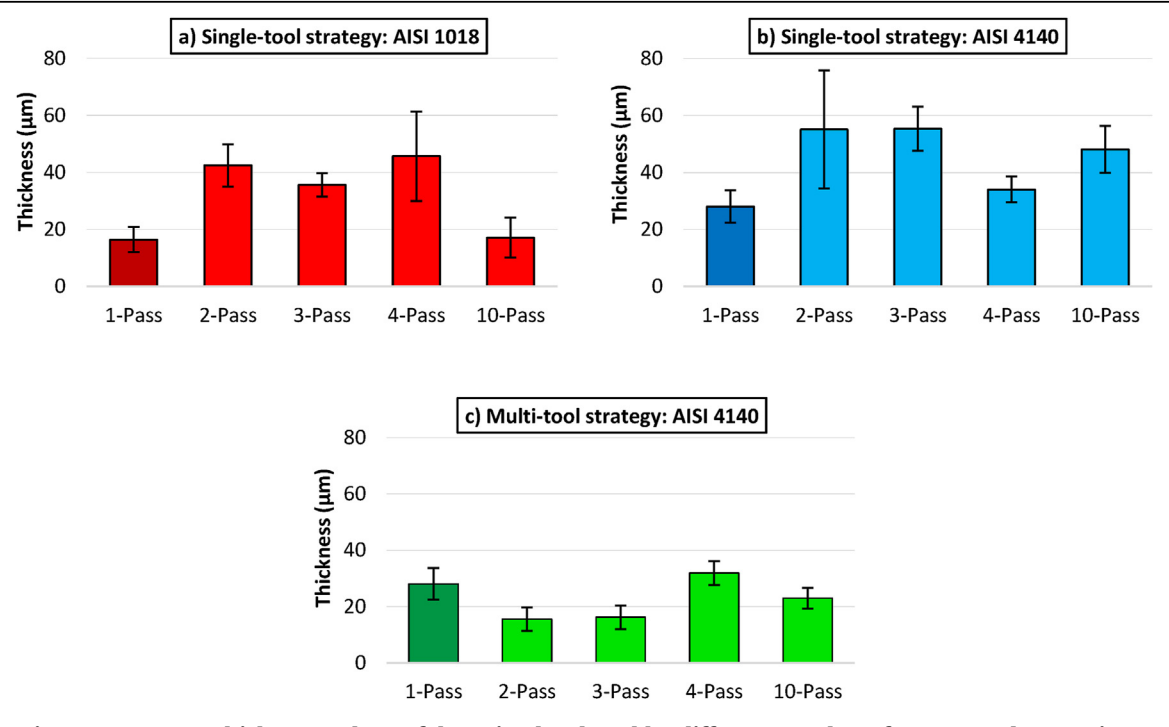


Fig. 12 - Average thickness values of deposits developed by different number of passes and strategies.

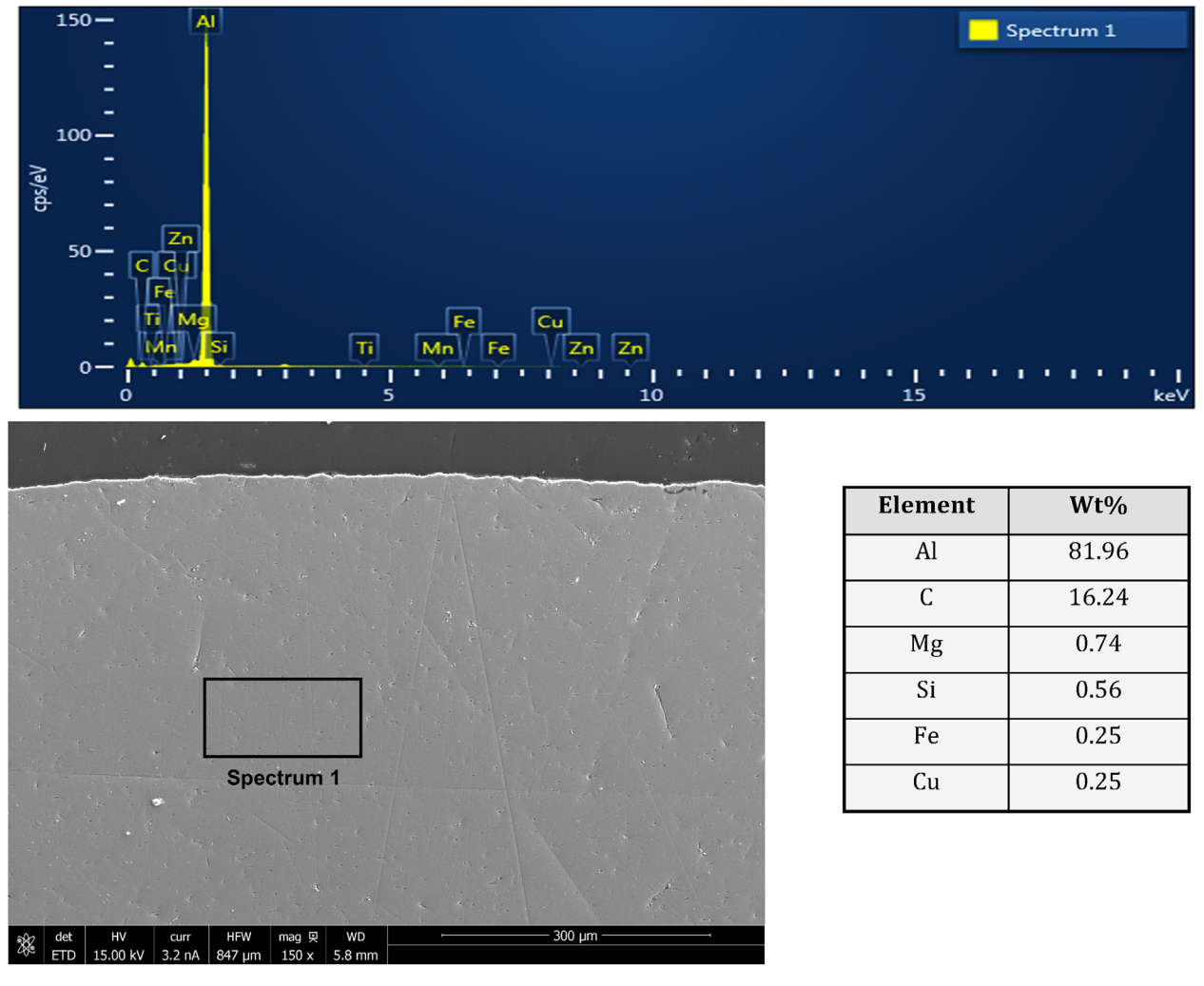
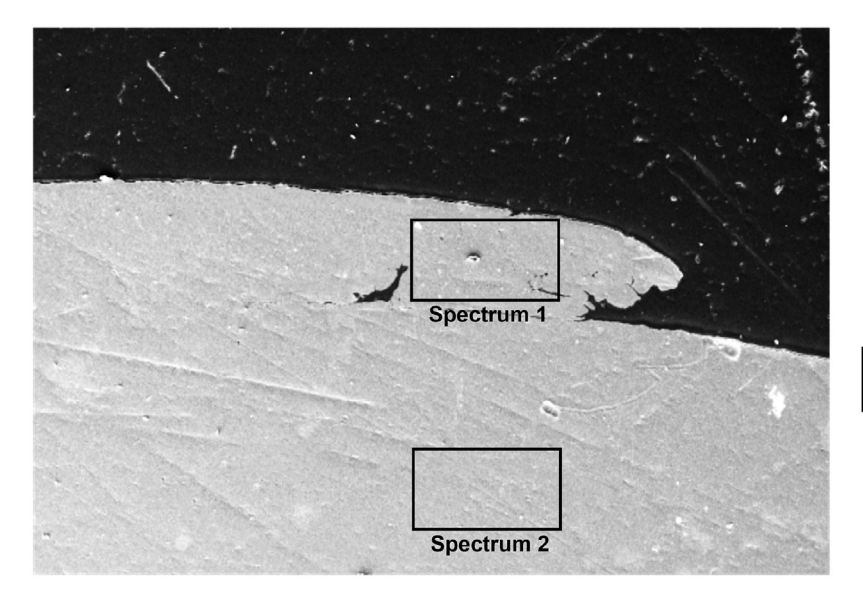


Fig. 13 - Cross section SEM imaging and EDS spectrum results of unused AA6061 rod utilized as consumable tool.



	Wt% of Fe	At% of Fe
Spectrum 1	1.26	0.61
Spectrum 2	0.44	0.21

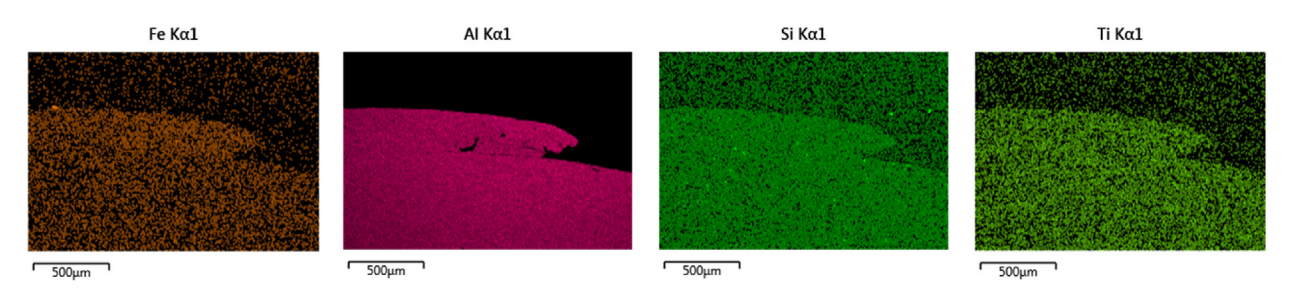


Fig. 14 - Cross section SEM imaging and EDS maps of used AA6061 rod.

generation rate in the multi-tool strategy was high enough to lead to an increasing process temperature trend, even though the substrate was cooling down during a time gap of 1 min required for rod replacement.

# 3.3. Surface roughness

500μm

Surface roughness was measured at 20 random spots on each sample, and the average roughness value (Ra) of the specimens are exhibited in Fig. 10. The error bars represent the standard deviations of the recorded values from the means. The surface roughness (Ra) of AISI 1018 and AISI 4140 substrates was 0.66  $\mu m$  and 4.8  $\mu m$ , respectively. The large difference in surface roughness values of these two types of substrates provides a better condition to assess the influence of substrate surface roughness on the quality of the coatings deposited through the multi-pass deposition process.

Fig. 10 shows that the surface roughness decreases after the first surfacing pass. After the fourth pass of deposition through the single-tool strategy, the surface roughness of coatings deposited onto AISI 1018 and AISI 4140 substrates decreases to 0.34  $\mu m$  and 2.32  $\mu m$ , respectively. On the other hand, multi-tool deposition resulted in a smoother coating with a roughness of 1.58  $\mu m$ . Deposition of extra passes up to 3 layers generally decreases the roughness values of the

surface; however, there are some fluctuations in the general decreasing trend of roughness values in the deposition of AA6061 onto AISI 1018 substrate. The minimum roughness value for all the deposited samples was obtained in the 3-pass coatings, and deposition of the fourth layer increased the roughness. Comparing the results of two different employed strategies revealed that the multi-tool deposition results in lower surface roughness values in all the specimens. The results show that smooth coatings (~1  $\mu m$ ) can be fabricated, even smoother than the as-received substrate. Furthermore, increasing the number of passes to three resulted in smaller error. This indicates that a more consistent coating was deposited as the number of passes increased. This result is consistent with the visual assessment of the specimens.

### 3.4. Material deposition rate

Flash formation is a serious concern in the conventional FS approach and can waste 40 to 60 percent of the total consumable material [51], which is a gigantic waste of material and energy. On the other hand, no flash forms in surfacing from the lateral surface. Therefore, the consumed material can be simply measured by determining the rod volume reduction during the deposition process, as presented in Fig. 11. The result shows almost the same rate of material

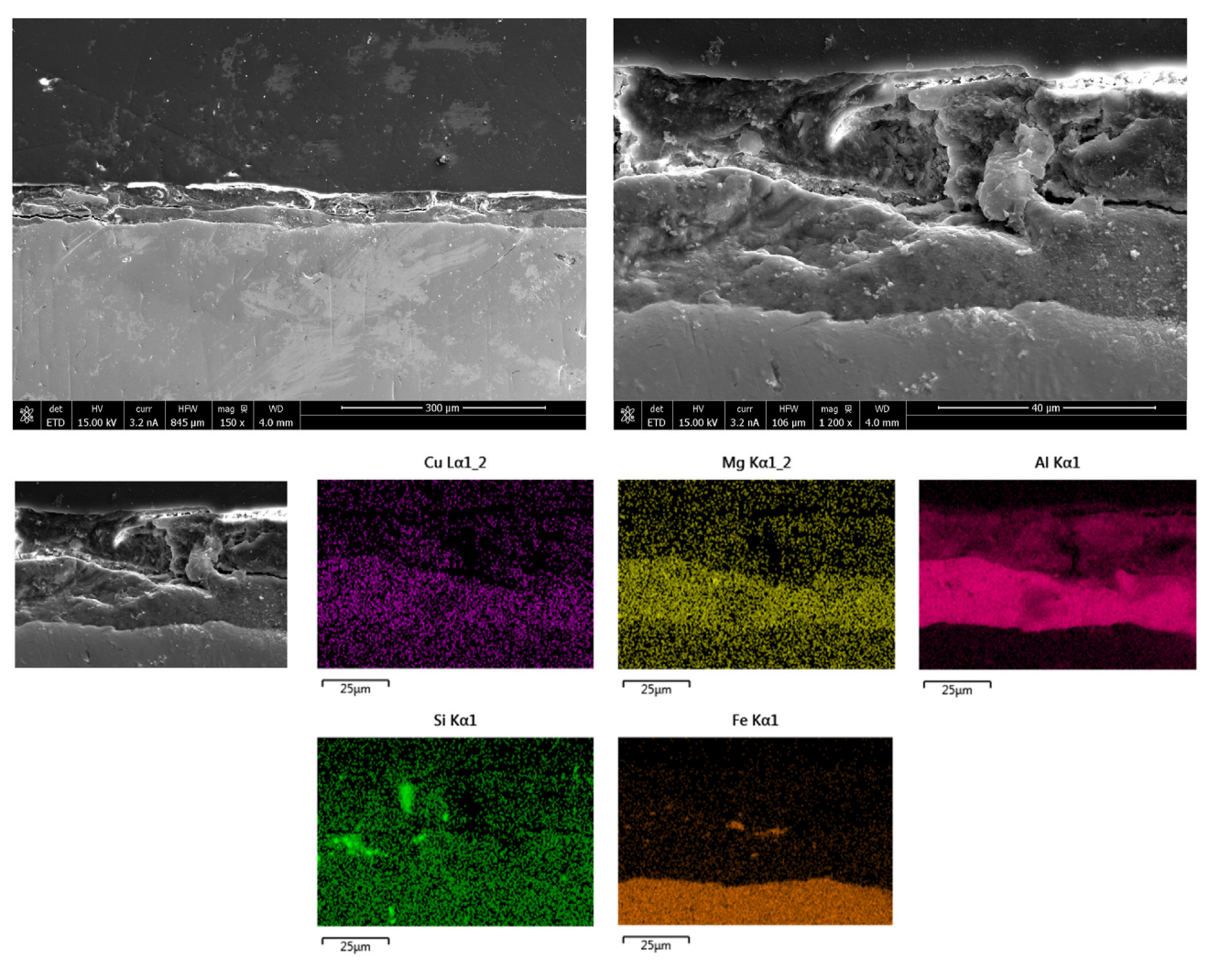


Fig. 15 - Single-pass deposition of AA6061 onto AISI 4140 through LFS.

consumption for deposition onto both substrates during the first layer deposition; however, a higher material deposition rate was recorded for deposition onto AISI 4140 substrate during the later passes. Generally, no specific trend for material deposition rate was observed during the multilayer deposition of AA6061 in these experiments.

In LFS, the first layer of the coating does not usually have good coverage. The upcoming deposition passes use consumable material to improve the coverage. After achieving complete coverage, no increment in material consumption was observed. This is proof that some portion of the deposited material transferred back to the lateral surface of the tool from the coating. As discussed before, this technique plasticizes a very thin layer of material on the lateral surface of the consumable rod. When this thin layer is deposited on the surface, the hard unplasticized area beneath that hits the previously deposited material directly, and can rub off the coating in the following tool revolution. This portion of material stick to the rod and will be deposited again in the next tool revolution when it returns to the tool/substrate interface.

Therefore, material can be transferred back and forth between the consumable tool and substrate, without increasing the material consumption rate. There was no trend of increasing coating thickness and material build up during the process because of this. The coating did become smoother and the coverage increased with increasing number of passes, while the final amount of material deposited was nearly the same as in first three layers.

The average thickness of fabricated deposits was extracted from measuring the thickness of 50 random points on the cross-section of each specimen, as shown in Fig. 12. The result of cross-sectional optical microscopy revealed that deposition of multiple successive layers of AA6061 does not necessarily increase the thickness of the deposits, and it may remove previously fabricated deposits. Deposition of the second layer through the single-tool strategy increased the coating thickness, while the coating thickness decreased in the multi-tool strategy. Depositing ten consecutive passes of the coating via the single-tool strategy onto AISI 1018 and AISI 4140 substrates produced coatings with the same and higher thickness

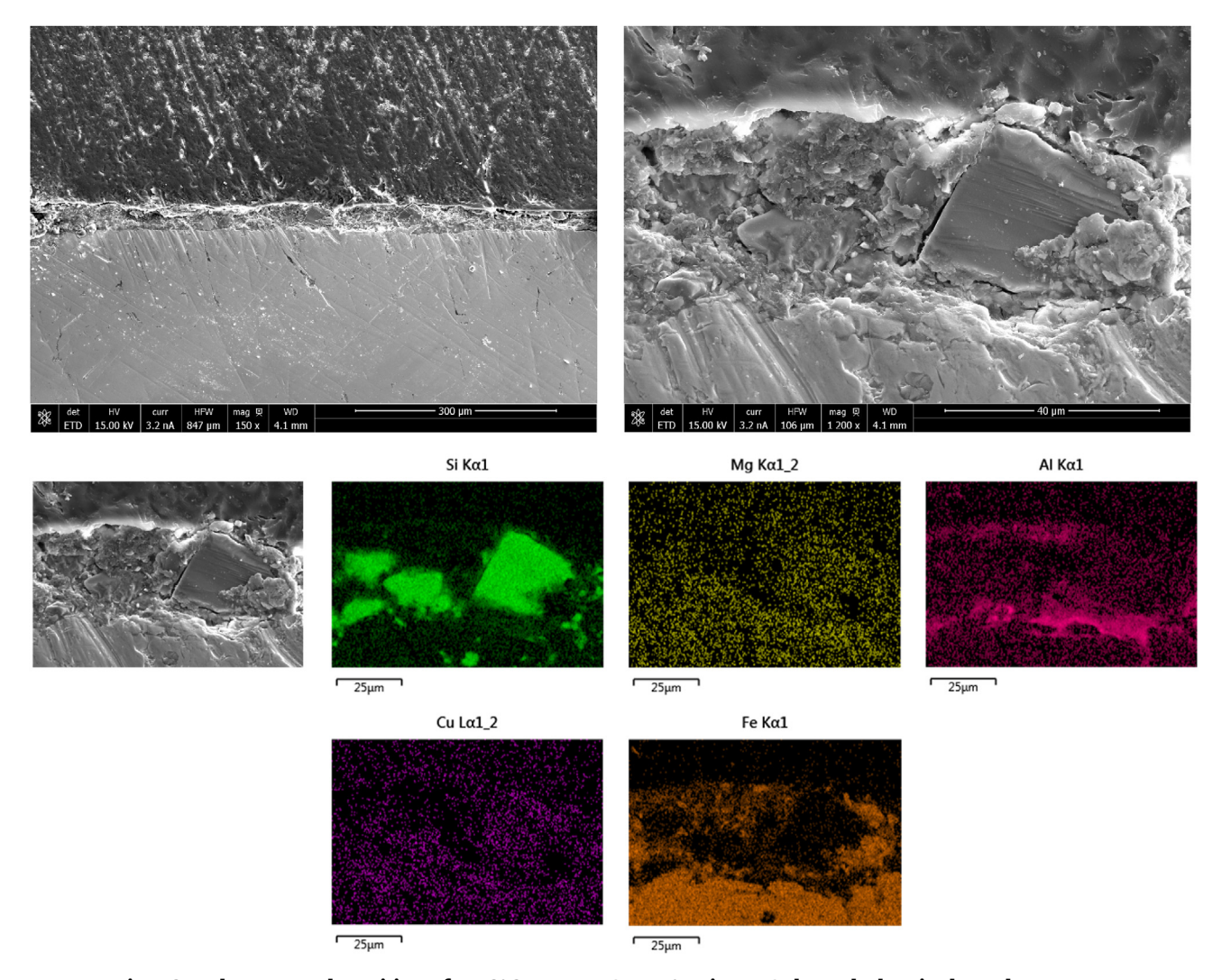


Fig. 16 - Three-pass deposition of AA6061 onto AISI 4140 using LFS through the single-tool strategy.

values compared to the first layer, respectively, while a lower coating thickness was obtained through the multi-tool strategy. These results revealed that the final thickness values are comparable to those of the first deposited layer.

# 3.5. Scanning electron microscopy and energy-dispersive X-ray spectroscopy

The multi-pass deposition was characterized using SEM and EDS analyses. For this purpose, 1, 3, and 10 pass deposition of AA6061 onto AISI4140 as well as the used and as-received AA6061 rod were subjected to SEM and EDS analyses. Analyzing the as-received materials is crucial to understanding the origin of elements or possible defects inside the deposits.

3.5.1. Used and as-received AA6061 consumable rods
Fig. 13 presents the result of cross-sectional SEM imaging, EDS
spectrum, and elemental percentage of the as-received
AA6061 consumable tool. The higher volume of carbon reported in this examination is due to the epoxy and the polishing agents in polycrystalline diamond suspension, which

may remain on the surfaces after polishing and washing process. Fig. 14 presents the cross-section SEM imaging and EDS maps of the AA6061 rod used for fabrication of the second pass through the multi-tool strategy. The wave-like shape region on the radial surface of the rod clearly shows the shearing flow of the plasticized material. In order to examine the reverse material transfer during the process, two regions on the shearing flow and the inner area of the rod were subjected to EDS analysis. The EDS maps and the elemental percentage evaluation revealed that the presence of iron on the lateral surface of the rod is almost three times more than that in the inner regions of the rod, indicating migration of Fe element through a reverse material transfer from the coating onto the rod radial surface.

3.5.2. Specimens fabricated through single-pass deposition The cross-section SEM imaging and EDS elemental mapping of single-pass AA6061 deposition onto AISI 4140 is presented in Fig. 15. The SEM images show a complete bonding at the coating and substrate interface; however, large cracks were observed in several regions on the coating cross-section, acting as a boundary and dividing the deposit into two

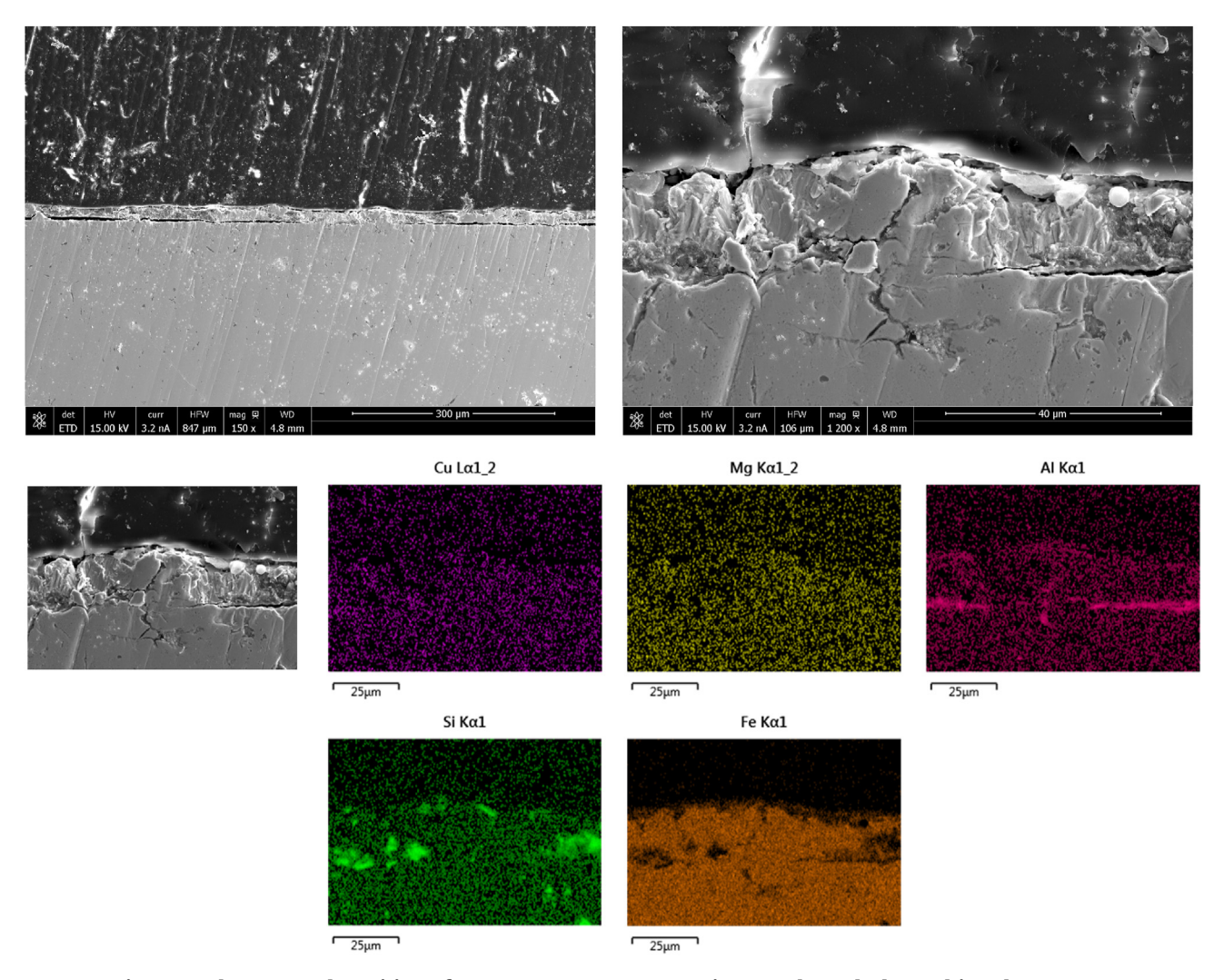


Fig. 17 - Three-pass deposition of AA6061 onto AISI 4140 using LFS through the multi-tool strategy.

different areas. The layer at the bottom looks like a dense layer, but the second top part of the layer has pores and cracks. The EDS analysis revealed two different deposit phases with different elemental percentages generated at the top and bottom of the fabricated coating. The half bottom of the deposit consists of more aluminum, magnesium, and copper elements, while the half top part of the coating had more carbon. The majority of carbon detected in the EDS analysis of the deposits is due to the thin layer of graphite added to the substrate surface as well as the epoxy and diamond polishing particles. Moreover, small silicon-rich areas were detected in the coating, while such regions were not observed in the asreceived tool. It has been reported that silicon has low solubility in aluminum; therefore, this element precipitates and forms almost pure silicon regions [52].

3.5.3. Specimens fabricated through three-pass deposition The cross-section SEM imaging and EDS elemental mapping of three-pass deposition of AA6061 onto AISI 4140 through the first and second strategies are presented in Figs. 16 and 17, respectively. The deposition through the single-tool strategy has resulted in a complete bonding between deposit and steel

plate, and no crack or pores at the interface was observed. Nevertheless, the EDS maps revealed several large chunks of silicon generated inside the coating. Such large silicon chunks were not observed in the consumable material; therefore, they must have been formed during the deposition process. The formation of such large segments can cause cracks and lessen the deposit strength. In addition, aluminum was more concentrated at the interface of the deposit/substrate, showing a higher bonding capability between aluminum and steel. Moreover, iron from the substrate was detected in the coating, indicating material transferring between the substrate and deposit. The rotating tool rubs the substrate surface and transfers the elements inside the substrate to the coating.

On the other hand, in the multi-tool strategy, a slightly thinner layer of deposit was fabricated in three-pass deposition showing unbonded regions at the majority of the interface. Moreover, the smaller silicon-rich areas were noticed compared to the three-pass deposit fabricated by single-tool strategy. A concentration of iron was observed inside the coating, due to the fact that newly employed rods at each pass is harder compared to the used rods, resulting in more abrasion and material transferring from the steel substrate to the

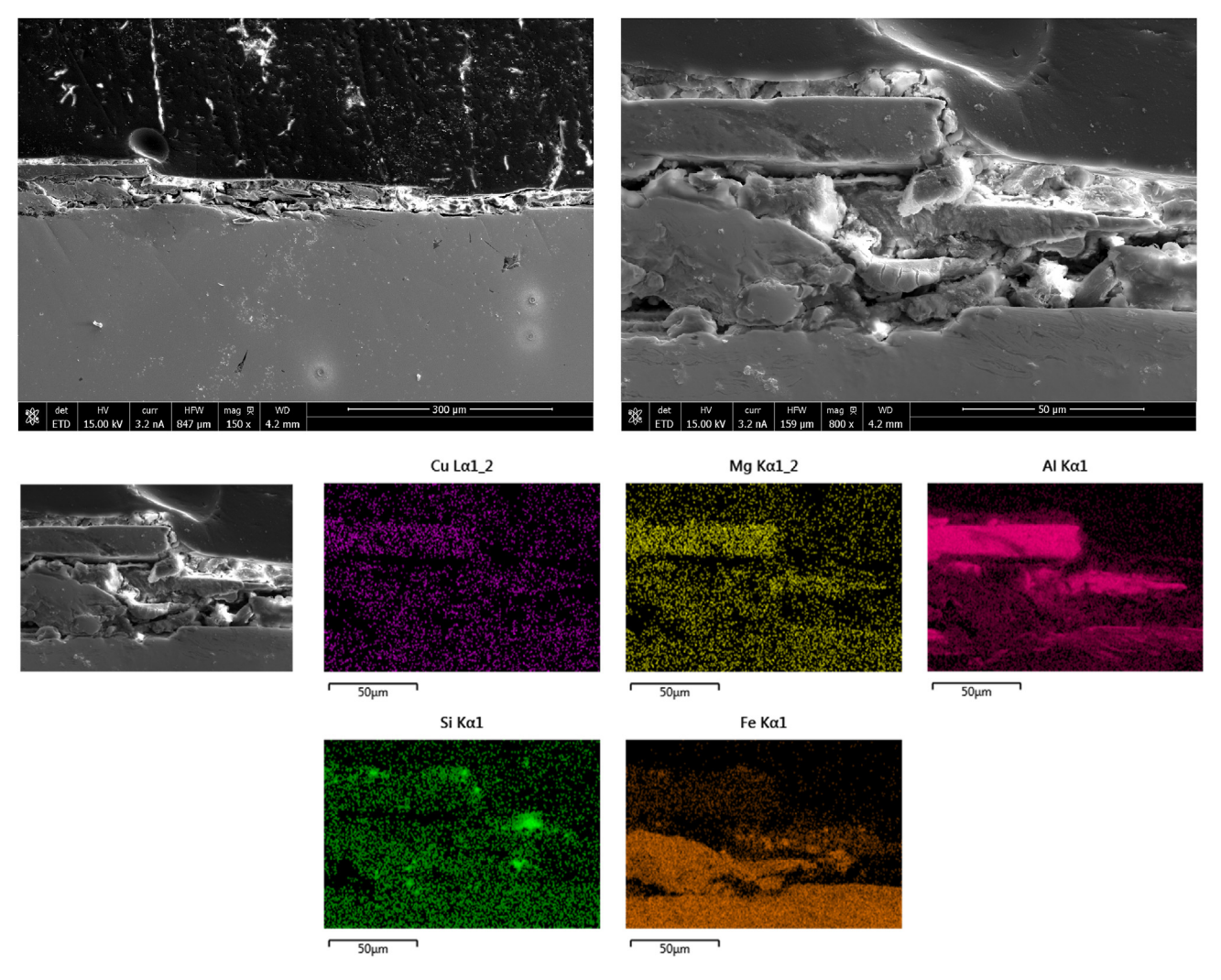


Fig. 18 - Ten-pass deposition of AA6061 onto AISI 4140 using LFS through the single-tool strategy.

deposit. The multi-pass deposition with multi-tool strategy seemed to cause more damage to the surface initially and then deposit a mix of substrate and consumable material, instead of depositing aluminum alloy alone.

Specimens fabricated through ten-pass deposition Figs. 18 and 19 present the result of cross-section SEM imaging and EDS elemental mapping of ten-pass deposition of AA6061 onto AISI 4140 through the first and second strategies, respectively. The ten-pass deposition through the single-tool strategy resulted in formation of different separated phases in the deposit. Similar to the previous samples, accumulation of Fe and Si elements was detected in this sample. Moreover, an aluminum layer was detected on top of the coating, which has been fabricated in the last passes of deposition, as shown in Fig. 18. Increasing the number of passes up to ten passes applied stress and vibration in the previously bonded coating which can result in formation of cracks at the interface of coating and substrate. On the other hand, the multi-tool strategy resulted in more consistent deposition in term of thickness and internal material phases. As was discussed in the three-pass deposition, multi-tool strategy resulted in a

deposit which consisted of a large amount of iron. Also, concentration of aluminum was detected at the interface of the coating and substrate.

As shown in Figs. 15, 18 and 19, the thickness of the singlepass and 10-pass coatings are comparable. Only a thin layer of material can be plasticized on the lateral side of the consumable tool due to low process temperature; therefore, only this thin plasticized layer can be deposited on the substrate, after which, the unplasticized area beneath can rub off the deposited material in the following tool revolution due to harder tool surface or presence of pores and cracks in the deposited coating. This removed plasticized material sticks to the rod, and can be redeposited later. The SEM results indicate that the substrate surface was rubbed off too, resulting in transferring Fe from the substrate to the coating as the number of passes increases, as shown in Figs. 15, 16 and 18. This phenomenon will be repeated regularly, and the fabricated material in the first pass sticks to the rod and will be deposited again regularly.

This phenomenon is more noticeable in the multi-tool strategy when a fresh rod was employed in each pass, as shown in Figs. 17 and 19. This is because the surface of the as-

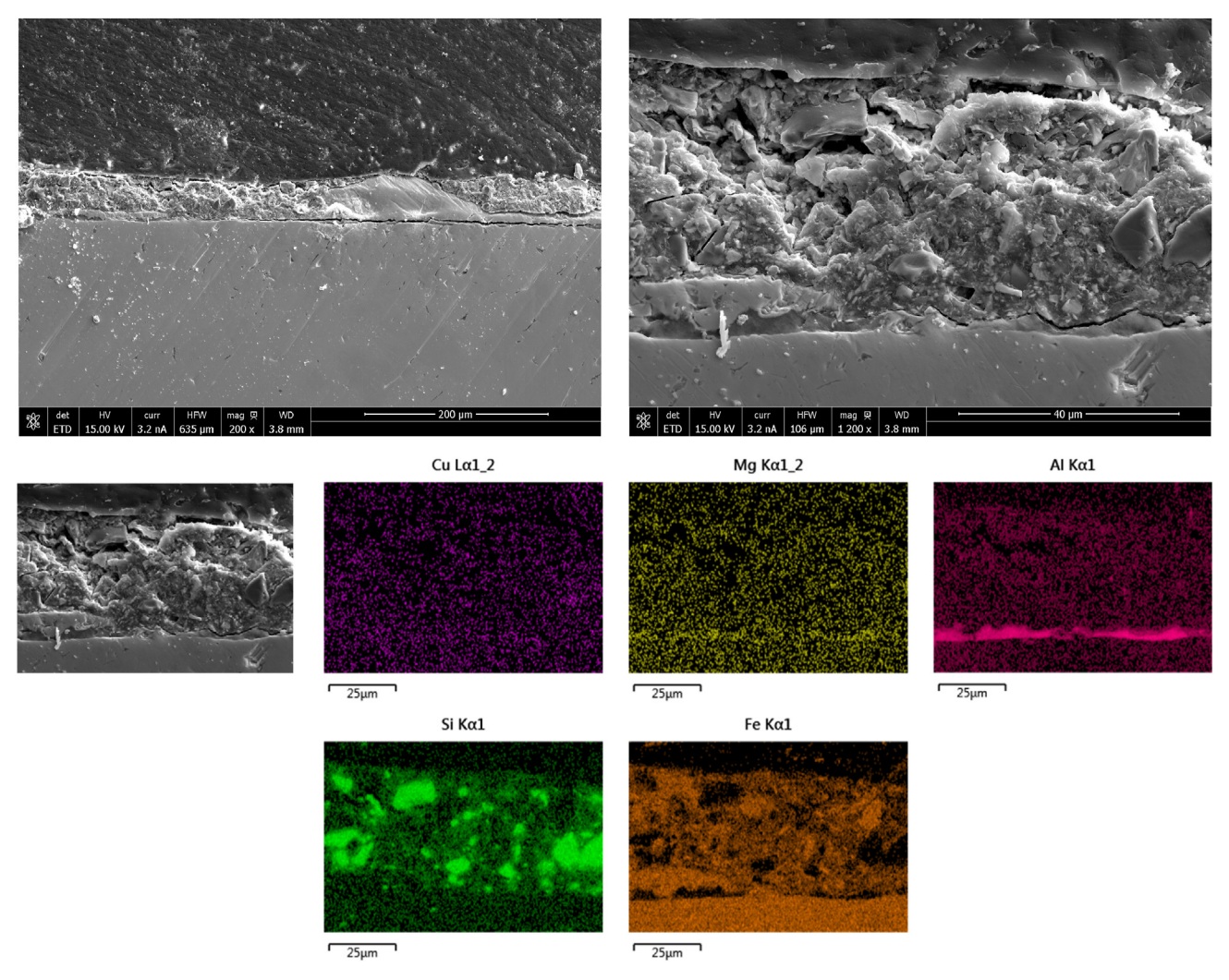


Fig. 19 - Ten-pass deposition of AA6061 onto AISI 4140 using LFS through the multi-tool strategy.

received rod is harder than the surface of a used rod as some portion of the deposited coating material has stuck on its surface. Hence, the hard surface of a fresh and cold tool can rub off the coating and substrate surface more severely. That is why concentration of Fe element was more detected in every deposited coating via the multi-tool strategy. There is a question that, despite of the reverse material transferring process, how the material deposition rate of AA6061 onto AISI4140 increased significantly in the second pass. The answer to this question is rooted in Fig. 4, where the physical appearance of the deposited samples is presented. As shown in Fig. 4, the single-pass deposition onto the AISI 4140 substrate does not have good coverage. Therefore, the rotating rod is still working on depositing consumable material on the hard steel substrate during the second pass. After reaching better coverage in the second pass, the back and forth transferring of consumable materials between rod and substrate is quite noticeable, as shown in Fig. 11. It was also revealed that further material deposition from the rod onto substrate can still occurs if a strong and hard base layer is provided in the previous pass. This phenomenon can be observed in Fig. 18,

where an aluminum-rich layer is fabricated on an iron-rich region.

## 4. Conclusion

In this study, the recently introduced approach of FS from the lateral surface of the consumable rod was adopted to assess the potential application of this technique for fabricating multilayer deposits and additive manufacturing purposes. The mechanical properties and metallurgical characteristics of the deposits were evaluated to study the effects of single/multi-tool strategy, multi-pass deposition, and different materials. The prominent results of this study can be concluded as follows:

 The multi-pass deposition of AA6061 through LFS did not result in a trend of increasing coating thickness due to the formation of a reverse material transferring process from the coating to the radial surface of the rod. The final thickness obtained from the 10-pass deposition was

- comparable to the average thickness values of the first and second passes.
- Coating fabrication through the LFS approach resulted in material transfer from the substrate to the deposit due to the elevated stress and temperature. This phenomenon happened more severely through employing a new tool for the deposition of each pass, resulting in large iron-rich areas inside the coating.
- Fabrication of multi-pass coating through LFS technique resulted in smooth and consistent coating layer. A complete coverage on both utilized substrate materials was achieved in the fourth pass of deposition.
- By fabricating further deposition passes, increment in force ratio was observed. The tangential force increases until it converges to normal force during deposition of the fourth pass and reaches a steady state.
- The maximum process temperature decreases at some point during the multi-pass deposition using a single rod; however, the maximum process temperature continuously increases in deposition through a fresh rod in each pass.
- The surface hardness of the tools decreased during the deposition through LFS. The tool can rub off the deposited coating, then some portion of the plasticized material can be transferred back to the tool, resulting in a softer layer on the radial surface of the tool. Material gets churned up in the transfer between tool and substrate, creating layers and areas rich in silicon due to the precipitation of this element during the process.

# **Declaration of Competing Interest**

The authors declare that they have no known competing financial interests or personal relationships that could have appeared to influence the work reported in this paper.

## Acknowledgments

The work was supported by National Science Foundation CMMI grant #1763147, Office of Naval Research award #N000142112861, and General Motors.

#### REFERENCES

- [1] Palanivel S, Mishra RS. Building without melting: a short review of friction-based additive manufacturing techniques. Int J Addit Subt Mat Manuf 2017;1(1):82–103.
- [2] Seidi E, Miller SF. Friction surfacing using consumable tools: a review. Proc ASME 2019 14th Int Manuf Sci Eng Conf 2019;2:V002T03A048.
- [3] Gandra J, Krohn H, Miranda RM, Vilaça P, Quintino L, Dos Santos JF. Friction surfacing—a review. J Mater Process Technol 2014;214(5):1062–93.
- [4] Seidi E, Miller SF, Carlson BE. Friction surfacing deposition by consumable tools. J Manuf Sci Eng 2021;143(12):120801.
- [5] Pirhayati P, Aval HJ. An investigation on thermo-mechanical and microstructural issues in friction surfacing of Al—Cu aluminum alloys. Mater Res Express 2019;6(5):056550.

- [6] Phillips BJ, Avery DZ, Liu T, Rodriguez OL, Mason CJT, Jordon JB, et al. Microstructure-deformation relationship of additive friction stir-deposition Al–Mg–Si. Materialia 2019;7:100387.
- [7] Isupov FY, Panchenko OV, Naumov AA, Alekseeva MD, Zhabrev LA, Popovich AA. Consumable tool for coating deposition by joint deformation of the base and tool materials. Russ Metall 2019;(13):1399–406.
- [8] Pereira D, Gandra J, Pamies-Teixeira J, Miranda RM, Vilaça P. Wear behaviour of steel coatings produced by friction surfacing. J Mater Process Technol 2014;214(12):2858–68.
- [9] Fitseva V, Krohn H, Hanke S, Dos Santos JF. Friction surfacing of Ti–6Al–4V: process characteristics and deposition behaviour at various rotational speeds. Surf Coating Technol 2015;278:56–63.
- [10] Dovzhenko G, Hanke S, Staron P, Maawad E, Schreyer A, Horstmann M. Residual stresses and fatigue crack growth in friction surfacing coated Ti-6Al-4V sheets. J Mater Process Technol 2018;262:104–10.
- [11] Silva KHS, Brito PP, Santos IB, Câmara MA, Abrão AM. The behaviour of AISI 4340 steel coatings on low carbon steel substrate produced by friction surfacing. Surf Coating Technol 2020;399:126170.
- [12] Kallien Z, Rath L, Roos A, Klusemann B. Experimentally established correlation of friction surfacing process temperature and deposit geometry. Surf Coat Technol 2020:126040.
- [13] Galvis JC, Oliveira PHF, Martins JDP, Carvalho ALMD. Assessment of process parameters by friction surfacing on the double layer deposition. Mater Res 2018;21(3):e20180051.
- [14] Huang YX, Han B, Lv SX, Feng JC, Liu HJ, Leng JS, et al. Interface behaviours and mechanical properties of filling friction stir weld joining AA 2219. Sci Technol Weld Join 2012;17(3):225–30.
- [15] Han B, Huang Y, Lv S, Wan L, Feng J, Fu G. AA7075 bit for repairing AA2219 keyhole by filling friction stir welding. Mater Des 2013;51:25–33.
- [16] Hanke S, Fischer A, dos Santos JF. Sliding wear behaviour of a Cr-base alloy after microstructure alterations induced by friction surfacing. Wear 2015;338:332–8.
- [17] Vasanth R, Mohan K, Rengarajan S, Jayaprakash R, Kumar RA. Characterization and corrosion effects of Friction surfaced IS-2062 E250 CU with AA6063. Mater Res Express 2019;6(12):126579.
- [18] Sudherson DPS, Anandkumar PP, Jinu GR, Balasubramanian KA, Vettivel SC. Experimental investigation on corrosion behavior of friction surfaced mild steel with aluminum alloy 5083-Cadmium composite. Mater Res Express 2019;6(8):086587.
- [19] Bararpour SM, Aval HJ, Jamaati R. An experimental and theoretical investigation of thermo-mechanical issues in friction surfacing of Al–Mg aluminum alloys: material flow and residual stress. Model Simulat Mater Sci Eng 2020;28(3):035003.
- [20] Guo D, Kwok CT, Chan SLI. Spindle speed in friction surfacing of 316L stainless steel—How it affects the microstructure, hardness and pitting corrosion resistance. Surf Coating Technol 2019;361:324—41.
- [21] Galvis JC, Oliveira PHF, Hupalo MF, Martins JP, Carvalho ALM. Influence of friction surfacing process parameters to deposit AA6351-T6 over AA5052-H32 using conventional milling machine. J Mater Process Technol 2017;245:91–105.
- [22] Troysi F, Silva K, Santos ÍD, Brito P. Investigation of austenitic stainless steel coatings on mild steel produced by friction surfacing using a conventional CNC machining center. Mater Res 2019;22(2):e20180301.
- [23] Kumar BV, Reddy GM, Mohandas T. Influence of process parameters on physical dimensions of AA6063 aluminium

- alloy coating on mild steel in friction surfacing. Defence Technol 2015;11(3):275–81.
- [24] Rafi HK, Ram GJ, Phanikumar G, Rao KP. Friction surfaced tool steel (H13) coatings on low carbon steel: a study on the effects of process parameters on coating characteristics and integrity. Surf Coating Technol 2010;205(1):232—42.
- [25] Rathee S, Srivastava M, Maheshwari S, Kundra TK, Siddiquee AN. Friction based additive manufacturing technologies: principles for building in solid state, benefits, limitations, and applications. CRC Press; 2018.
- [26] Dilip JJS, Babu S, Rajan SV, Rafi KH, Ram GJ, Stucker BE. Use of friction surfacing for additive manufacturing. Mater Manuf Process 2013;28(2):189–94.
- [27] Karthik GM, Ram GJ, Kottada RS. Friction deposition of titanium particle reinforced aluminum matrix composites. Mater Sci Eng A 2016;653:71–83.
- [28] Tokisue H, Katoh K, Asahina T, Usiyama T. Mechanical properties of 5052/2017 dissimilar aluminum alloys deposit by friction surfacing. Mater Trans 2006;47(3):874–82.
- [29] MELD brochure, Aeroprobe corporation. 2018. Available from, http://www.aeroprobe.com/meld/.
- [30] Khodabakhshi F, Gerlich AP. Potentials and strategies of solid-state additive friction-stir manufacturing technology: a critical review. J Manuf Process 2018;36:77–92.
- [31] Anderson-Wedge K, Avery DZ, Daniewicz SR, Sowards JW, Allison PG, Jordon JB, et al. Characterization of the fatigue behavior of additive friction stir-deposition AA2219. Int J Fatig 2021;142:105951.
- [32] Garcia D, Hartley WD, Rauch HA, Griffiths RJ, Wang R, Kong ZJ, et al. In situ investigation into temperature evolution and heat generation during additive friction stir deposition: a comparative study of Cu and Al-Mg-Si. Addit Manuf 2020;34:101386.
- [33] Yu HZ, Jones ME, Brady GW, Griffiths RJ, Garcia D, Rauch HA, et al. Non-beam-based metal additive manufacturing enabled by additive friction stir deposition. Scripta Mater 2018;153:122–30.
- [34] Rivera OG, Allison PG, Brewer LN, Rodriguez OL, Jordon JB, Liu T, et al. Influence of texture and grain refinement on the mechanical behavior of AA2219 fabricated by high shear solid state material deposition. Mater Sci Eng A 2018;724:547–58.
- [35] Griffiths RJ, Petersen DT, Garcia D, Yu HZ. Additive friction stir-enabled solid-state additive manufacturing for the repair of 7075 aluminum alloy. Appl Sci 2019;9(17):3486.
- [36] Griffiths RJ, Garcia D, Song J, Vasudevan VK, Steiner MA, Cai W, et al. Solid-state additive manufacturing of aluminum and copper using additive friction stir deposition: processmicrostructure linkages. Materialia 2021;15:100967.
- [37] Rutherford BA, Avery DZ, Phillips BJ, Rao HM, Doherty KJ, Allison PG, et al. Effect of thermomechanical processing on fatigue behavior in solid-state additive manufacturing of Al-Mg-Si alloy. Metals 2020;10(7):947.

- [38] Priedeman JL, Phillips BJ, Lopez JJ, Tucker Roper BE, Hornbuckle BC, Darling KA, et al. Microstructure development in additive friction stir-deposited Cu. Metals 2020;10(11):1538.
- [39] Avery DZ, Rivera OG, Mason CJT, Phillips BJ, Jordon JB, Su J, et al. Fatigue behavior of solid-state additive manufactured inconel 625. J Occup Med 2018;70(11):2475–84.
- [40] Rivera OG, Allison PG, Jordon JB, Rodriguez OL, Brewer LN, McClelland Z, et al. Microstructures and mechanical behavior of Inconel 625 fabricated by solid-state additive manufacturing. Mater Sci Eng A 2017;694:1—9.
- [41] Li B, Shen Y, Lei L, Hu W. Fabrication and evaluation of Ti3Alp/Ti-6Al-4V surface layer via additive friction-stir processing. Mater Manuf Process 2014;29(4):412-7.
- [42] McClelland Z, Avery DZ, Williams MB, Mason CJT, Rivera OG, Leah C, et al. Microstructure and mechanical properties of high shear material deposition of rare earth magnesium alloys WE43. In: Magnesium technology; 2019. p. 277–82.
- [43] Griffiths RJ, Perry MEJ, Sietins JM, Zhu Y, Hardwick N, Cox CD, et al. A perspective on solid-state additive manufacturing of aluminum matrix composites using MELD. J Mater Eng Perform 2019;28(2):648–56.
- [44] Seidi E, Miller SF. A novel approach to friction surfacing: experimental analysis of deposition from radial surface of a consumable tool. Coatings 2020;10(11):1016.
- [45] Seidi E, Miller SF. Friction surfacing from radial surface of A6063 aluminum alloy consumable tool onto A36 carbon steel. Proc ASME 2020 Int mech eng congress expos 2020;2A. Advanced manufacturing, virtual, V02AT02A003.
- [46] Seidi E, Miller SF. Lateral friction surfacing: experimental and metallurgical analysis of different aluminum alloy depositions. J Mater Res Technol 2021;15:5948–67.
- [47] Seidi E, Miller SF. Characterization of lateral friction surfaced AA6063 coatings. Proc ASME 2021 Int mech eng congress expos 2021; Volume 3. Advanced Materials: Design, Processing, Characterization, and Applications. Virtual, Online. November 1–5, V003T03A040.
- [48] Relue W, Seidi E, Hihara LH, Miller SF. Corrosion performance of different aluminum alloy deposits fabricated by lateral friction surfacing. Proc ASME 2021 Int mech eng congress expos 2021;3. Advanced Materials: Design, Processing, Characterization, and Applications. Virtual, Online. November 1–5, V003T03A029.
- [49] AZoM. March 1, 2022. Available from: https://www.azom.com.
- [50] Lambiase F, Paoletti A, Di Ilio A. Forces and temperature variation during friction stir welding of aluminum alloy AA6082-T6. Int J Adv Manuf Technol 2018;99:337–46.
- [51] Gandra J, Miranda RM, Vilaça P. Performance analysis of friction surfacing. J Mater Process Technol 2012;212(8):1676–86.
- [52] Cornell R, Bhadeshia HKDH. Aluminium-silicon casting alloys. Available from, http://www.phase-trans.msm.cam. ac.uk/abstracts/M7-8.html; March 1, 2022.